European Journal of
Mineralogy
Open Access

Pilanesbergite: a new rock-forming mineral occurring in nepheline syenite from the Pilanesberg Alkaline Complex, South Africa

Fabrice Dal Bo[1,2], **Henrik Friis**[1], **Marlina A. Elburg**[3], **Frédéric Hatert**[2], **and Tom Andersen**[1,3]

[1]Natural History Museum, University of Oslo, P.O. Box 1172, Blindern, 0318 Oslo, Norway
[2]Laboratory of Mineralogy B18, University of Liège, 4000 Liège, Belgium
[3]Department of Geology, University of Johannesburg, Auckland Park,
P.O. Box 524, 2066, Johannesburg, South Africa

Correspondence: Fabrice Dal Bo (fdalbo@uliege.be)

Abstract. The new mineral pilanesbergite, with the ideal formula $Na_2Ca_2Fe_2Ti_2(Si_2O_7)_2O_2F_2$, was found in a nepheline syenite, locally known as green foyaite, from the Pilanesberg Complex located in the North West Province of South Africa. Pilanesbergite occurs in green foyaite in association, and partly intergrown, with aegirine. The two minerals share an assemblage of inclusions, comprising euhedral nepheline, titanite and minor sodalite. Pilanesbergite belongs to the wöhlerite group and is isomorphic with låvenite, normandite and madeiraite. It is related to these species through the homovalent chemical substitutions $Mn^{2+} \leftrightarrow Fe^{2+}$ and $Zr^{4+} \leftrightarrow Ti^{4+}$. The empirical formula calculated on the basis of 18 anions is $Na_{2.00}(Ca_{1.74}Na_{0.26})_{\Sigma2.00}(Fe_{1.00}Mn_{0.52}Ca_{0.49}Zr_{0.05})_{\Sigma2.06}(Ti_{1.69}Zr_{0.14}Mg_{0.09}Nb_{0.08})_{\Sigma2.00}(Si_2O_7)_{2.00}O_{1.84}F_{2.16}$ ($Z = 2$). The new mineral is translucent with a brown orange colour and a brownish streak. The Mohs hardness is estimated between 5 and 6 by comparison with låvenite, and no cleavage is observed. Measured and calculated densities are $D_{meas} = 3.47\,\mathrm{g\,cm^{-3}}$ and $D_{calc} = 3.40\,\mathrm{g\,cm^{-3}}$. In the thin section the pleochroism is strong, between straw yellow and orange red, while in immersion the strong pleochroism is observed between light yellow (α) and yellowish orange (γ). The crystals are optically biaxial (+) with $\alpha = 1.743(3)$, $\beta = 1.768(3)$, $\gamma = 1.795(5)$ and a $2V$ angle close to 90°. The crystal structure is monoclinic ($P2_1/a$), with the unit-cell parameters $a = 10.7811(2)$, $b = 9.7836(1)$, $c = 7.0348(1)$ Å, $\beta = 108.072(2)°$ and $V = 705.41(2)$ Å^3, and has been refined to $R_1 = 2.06\%$. The strongest lines of the powder X-ray diffraction pattern [d, Å (I, %) ($h\,k\,l$)] are 3.219 (60) (310), 2.851 (100) (12-2), 2.802 (51) (320), 2.743 (27) (22-2), 2.423 (19) (40-2) and 1.723 (19) (44-2). Pilanesbergite formed under relatively reducing conditions from an agpaitic nepheline syenite magma that had evolved by fractional crystallization mainly of aegirine. Further crystallization of arfvedsonite caused an increase in oxygen fugacity and a change towards higher Mn/Mn + Fe of the magma, causing a change of mineral composition from pilanesbergite towards normandite.

1 Introduction

Pilanesbergite, ideally $Na_2Ca_2Fe_2Ti_2(Si_2O_7)_2O_2F_2$, was found in a syenite nepheline from the nearly circular Pilanesberg Complex, part of the Pilanesberg Alkaline Province, emplaced into the Palaeoproterozoic Bushveld Complex and located in the North West Province of South Africa. The complex is dated at 1395 ± 10 Ma based on LA-ICP-

MS U–Pb dating of titanite (Elburg and Cawthorn, 2017). The Pilanesberg Complex consists of different varieties of nepheline syenite (traditionally referred to as "foyaite"), with subordinate silica-saturated syenite, which intruded into their volcanic equivalents (Cawthorn, 2015). Pilanesbergite is hosted in a variety of nepheline syenite known as green foyaite, and the type material has been sampled from a natural exposure in a river gulley near the southern margin of

the complex at 25.3463° S, 27.0658° E. The rock containing pilanesbergite was collected by two of the authors (Tom Andersen, Marlina A. Elburg) and numbered MEPB62.

Pilanesbergite is a new member of the wöhlerite group (Dal Bo et al., 2022) and is isomorphic and chemically related to låvenite ($Na_2Ca_2Mn_2Zr_2(Si_2O_7)_2O_2F_2$) (Mellini, 1981), normandite ($Na_2Ca_2Mn_2Ti_2(Si_2O_7)_2O_2F_2$) (Perchiazzi et al., 2000) and madeiraite ($Na_2Ca_2Fe_2Zr_2(Si_2O_7)_2O_2F_2$) (Mills et al., 2021). The name, pilanesbergite, is based on the name of the type locality, the Pilanesberg Complex. The new mineral and name were approved by the Commission of New Minerals, Nomenclature and Classification of the International Mineralogical Association (proposal IMA2023-007). The cotype sample used for EPMA, structural refinement and petrographic description is deposited in the collection of the Natural History Museum, University of Oslo, NHM Økern, Kabelgata 38-40, 0580 Oslo, Norway (catalogue number KNR 44406). The cotype used for XPRD, optical properties and density measurement is stored in the mineralogical collection of the Laboratoire de Minéralogie, University of Liège, Belgium (catalogue no. 21980).

2   Occurrence and paragenesis

The rock is a medium-grained nepheline syenite showing flow foliation defined by parallel orientation of alkali feldspar crystals, now completely exsolved to end-member albite and microcline. Mafic silicate minerals (aegirine, sodic amphibole, titanite), eudialyte, lamprophyllite, pilanesbergite and minor pyrrhotite and Fe–Mn–Ti oxide minerals occur interstitially to feldspar and are enriched in bands parallel to the foliation. Pilanesbergite crystallized as a late magmatic mineral, together with aegirine and arfvedsonite, postdating alkali feldspar, nepheline and sodalite (Figs. 1, 2). The sample is heterogeneous on hand specimen and thin section scale, with pilanesbergite found in different textural relationships to other Ti-bearing minerals (Fig. 2). Pilanesbergite is in general associated, and partly intergrown, with aegirine. The two minerals share an assemblage of inclusions, comprising euhedral nepheline, titanite and minor sodalite. Titanite inclusions in aegirine have euhedral shapes; in pilanesbergite, they appear more irregular and are partly resorbed (Fig. 2c). Pilanesbergite has stable grain contacts with arfvedsonite, apatite and lamprophyllite (Fig. 2d, f). Associations of pilanesbergite and aenigmatite are less frequent in the sample and show variation: the two minerals occur intergrown suggesting simultaneous crystallization (Fig. 2a), and pilanesbergite and aenigmatite can replace titanite while remaining in stable contact with low-Ti aegirine (Fig. 2e). In contrast, some domains show pilanesbergite forming rims on resorbed aenigmatite crystals, suggesting a replacement relationship (Fig. 2b). Finally, pilanesbergite is itself replaced by Ti-enriched aegirine with ca. 10 wt % TiO_2, ex-

ceeding concentrations in the 2 wt % to 5 wt % range in primary magmatic aegirine in the sample (Fig. 2e). Lorenzenite forms scarce crystals in the sample, without grain contact with the other Ti-bearing minerals and appears to be associated with late-crystallized natrolite that rims and replaces nepheline. Aggregates of a fibrous Ti–Zr silicate mineral yet to be described are associated with the pilanesbergite. Sample MEPB62 has a $(Na + K)/Al$ ratio of 1.24, femic CIPW-normative minerals sum to 16.95 wt %; primary magmatic aegirine in the sample has 2 wt % to 6 wt % TiO_2 (Solem, 2019) and amphibole 2 wt %–2.5 wt %.

3   Physical and optical properties

The crystals are translucent with a brown orange colour and a brownish streak. The lustre is vitreous and the tenacity is brittle. The Mohs hardness is estimated between 5 and 6 by comparison with låvenite, and no cleavage is observed. Measured density determined with a Berman balance in toluene and calculated density are $D_{meas} = 3.47\,g\,cm^{-3}$ and $D_{calc} = 3.40\,g\,cm^{-3}$. In the thin section the pleochroism is strong, between straw yellow and orange red, while in immersion the strong pleochroism is observed between light yellow (α) and yellowish orange (γ). The refractive indices were determined by the immersion method by using Cargille refractive index liquids. The values of the refractive indices of the liquids were preliminary determined with a Leitz–Jelley refractometer using the 589 nm sodium light. The values of the refractive indices, determined under 589 nm light, are $\alpha = 1.743(3)$, $\beta = 1.768(3)$, $\gamma = 1.795(5)$ with a 2V angle close to 90° (2$V_{calc} = 88°$), and the crystals are optically biaxial (+). The optical orientation is not determined because the crystals cannot be oriented under the polarizing microscope due to the absence of cleavage planes. The Gladstone–Dale compatibility, $1 - (K_p/K_c)$, calculated from the EMPA data (Table 1), the measured density, and the measured refraction indices, is 0.037, which corresponds to the *excellent* category, according to Mandarino (1981).

4   Chemistry

The quantitative chemical analyses were performed using an electron microprobe CAMECA SX 100 equipped with four spectrometers and housed at the Spectrum Analytical Facility of the University of Johannesburg. The intensity data were corrected for matrix effects using the PAP procedure (Pouchou and Pichoir, 1991). The analytical conditions during collection were the following: wavelength dispersion mode, acceleration voltage of 15 kV, beam current of 15 nA, beam diameter of 5 μm and number of analyses of 15. The H_2O and CO_2 contents were not measured. The chemical composition of pilanesbergite is listed in Table 1 with respective standards for each element. The empirical formula calculated based on 18 anions (O + F) is
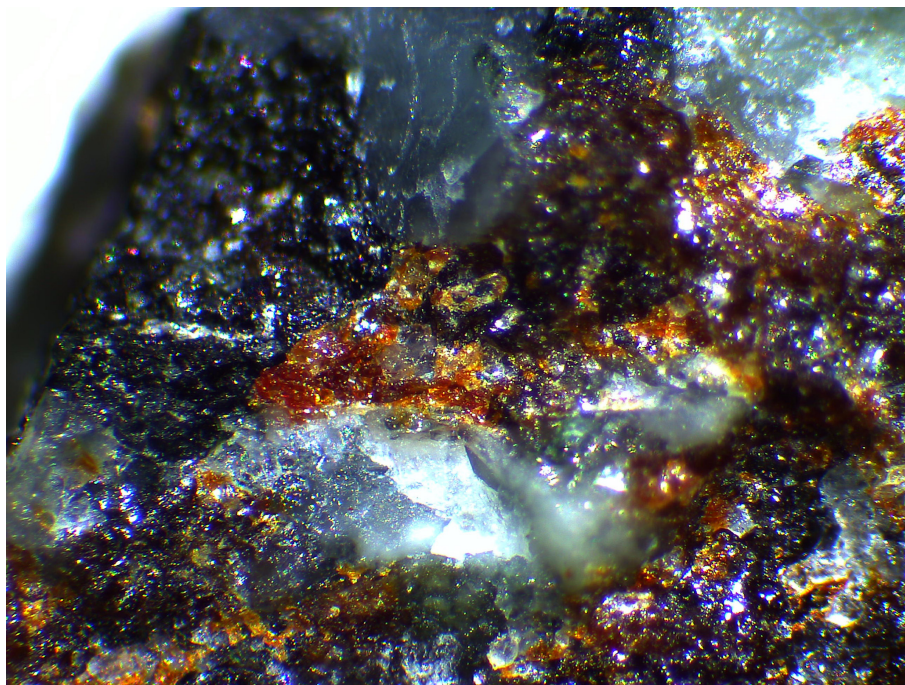
Figure 1. Brownish grains of pilanesbergite, associated with black aegirine and white feldspar. The width of the picture is 5 mm.

$Na_{2.00}(Ca_{1.74}Na_{0.26})_{\Sigma 2.00}(Fe_{1.00}Mn_{0.52}Ca_{0.49}Zr_{0.05})_{\Sigma 2.06}$ $(Ti_{1.69}Zr_{0.14}Mg_{0.09}Nb_{0.08})_{\Sigma 2.00}(Si_2O_7)_{2.00}O_{1.84}F_{2.16}$. The simplified formula is $Na_2(Ca,Na)_2(Fe,Mn,Ca,Zr)_2(Ti,Zr,Nb,Mg)_2(Si_2O_7)_2O_2F_2$, and the ideal formula is $Na_2Ca_2Fe_2Ti_2(Si_2O_7)_2O_2F_2$, which requires Na_2O 8.38, CaO 15.16, FeO 19.42, TiO_2 21.60, SiO_2 32.48, F 5.14 and $-F = O$ 2.16 for a total 100 wt %. The empirical formula shows a strong substitution of Fe^{2+} by Mn^{2+}, indicating an evolution of the pilanesbergite composition towards the normandite composition (Mn), as well as the incorporation of Ca^{2+} replacing Fe^{2+}. The slight substitution $Ti^{4+} \leftrightarrow Zr^{4+}$ indicates an evolution towards the madeiraite end-member composition.

5 X-ray diffraction

X-ray powder diffraction data were recorded at room temperature using a Bruker D8 Advance ECO diffractometer employing Cu$K\alpha$ radiation. Step-scan data were collected in the two-theta range 2 to 70° using a step size of 0.02° (Table 2). Pilanesbergite was the major phase including minor nepheline and microcline. Unit-cell parameters were refined in the $P2_1/a$ space group from the powder data using the LCLSQ8N software (Burnham, 1991) and are the following: $a = 10.761(7)$, $b = 9.756(7)$, $c = 7.020(4)$ Å, $\beta = 108.23(5)°$ and $V = 700.0(5)$ Å^3.

Single-crystal X-ray data were collected at room temperature with monochromated Mo$K\alpha$ radiation ($\lambda = 0.71703$ Å – 50 kV and 1 mA) on a Rigaku Synergy-S diffractometer

equipped with a HyPix-6000He detector housed at Natural History Museum, University of Oslo. The instrument has kappa geometry, and both data collection and subsequent data reduction and face-based absorption corrections were carried out using the CrysAlis Pro software (Oxford Diffraction, 2006). The details of the data collection and refinement are provided in Table 3. The initial structure solution in space group $P2_1/a$ was determined by the charge flipping method using the superflip algorithm (Palatinus and Chapuis, 2007), and the structural model was subsequently refined on the basis of F^2 with the Jana2006 software (Petříček et al., 2014). The structural model was started from the cation coordinates provided for normandite (Perchiazzi et al., 2000), and several refinement cycles and difference Fourier map calculations were performed to localize all the anionic sites of the structure. The site scattering factors were obtained by refining freely Ti at $X1$, Ca vs. Na at $X2$ and Fe vs. Ca at $X3$. Free refinement of $X4$ occupancy indicated that this site is fully occupied by Na. All atoms were refined with anisotropic thermal parameters, and those parameters as well as the atoms coordinates, bond distances, cation distribution and bond valence sums are provided in the Tables 4–7.

6 Discussions

6.1 Cation distribution and structural variation

Pilanesbergite is a new member of the wöhlerite group (Dal Bo et al., 2022). Its crystal structure is characterized by the
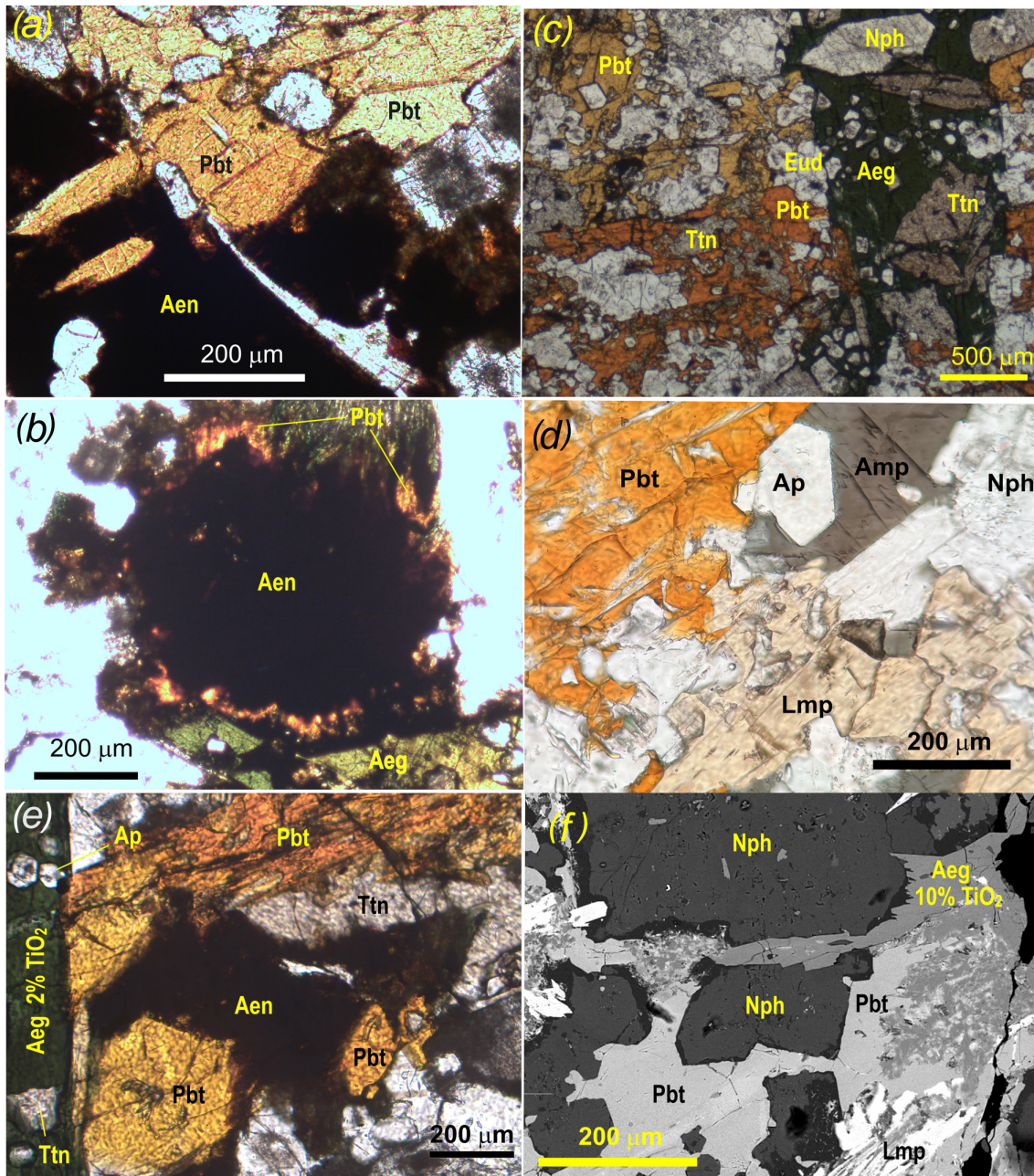
Figure 2. Photomicrographs showing mineral assemblages of pilanesbergite, sample MEPB62. **(a)** Intergrowths of pilanesbergite (*Pbt*) and aenigmatite (*Aen*) suggesting simultaneous crystallization and potential equilibrium between the two minerals. **(b)** The most abundant association in the sample, with titanite (*Ttn*) in stable coexistence with aegirine (*Aeg*), but being replaced by pilanesbergite (*Pbt*). **(c)** Pilanesbergite (*Pbt*) forming overgrowth on an aenigmatite crystal (*Aen*). **(d)** Pilanesbergite coexisting with amphibole (*Amp*), nepheline (*Nph*), apatite (*Ap*) and lamprophyllite (*Lmp*). There is no evidence of a reaction relationship between lamprophyllite and pilanesbergite. **(e)** Aenigmatite (*Aen*) and pilanesbergite (*Pbt*) replacing a heavily corroded titanite (*Ttn*) crystal. Both minerals appear to coexist with aegirine (*Aeg*) with ca. 2 wt % TiO_2 (semiquantitative analysis by SEM-EDS). Titanite inclusions in the aegirine show no evidence of replacement. **(f)** SEM-EDS photomicrograph of pilanesbergite (*Pbt*) interstitial to nepheline (*Nph*). Pilanesbergite coexists with lamprophyllite (*Lmp*), but is replaced by aegirine (*Aeg*) with ca. 10 % TiO_2. Dark rims on nepheline crystals consist of natrolite.

Table 1. Chemical data (wt %) for pilanesbergite.

Constituent (wt %)	Mean	Range	SD (2σ)	Reference material
SiO_2	32.28	31.88–32.62	0.37	Diopside
Al_2O_3	0.03	0.01–0.04	0.02	Almandine
TiO_2	18.33	17.63–19.12	0.94	Synthetic TiO_2
ZrO_2	2.95	2.19–4.16	1.10	Zircon
FeO	9.70	8.54–10.26	0.98	Hematite
MnO	4.96	4.62–5.52	0.52	Rhodonite
MgO	0.49	0.39–0.63	0.14	Olivine
CaO	16.87	16.27–17.64	0.79	Wollastonite
Na_2O	9.43	9.23–9.60	0.20	Jadeite
K_2O	0.01	0.00–0.02	0.01	Orthoclase
SrO	0.18	0.11–0.22	0.06	Celestine
Nb_2O_5	1.36	1.06–1.76	0.39	Pure metal
Ce_2O_3	0.02	0.00–0.08	0.05	Synthetic $CePO_4$
F	5.54	5.42–5.63	0.11	Fluorite
Total	102.13			
O=F	2.33			
Total	99.80			

so-called "octahedral walls" of four columns' width. The walls are interconnected through corner sharing and via the disilicate groups to create a framework structure (Fig. 3). The structure contains four cationic ($X1$–$X4$) and two anionic ($W1$–$W2$) sites that are affected by heterovalent substitutions. Based on the site-scattering values and the average bond distances (Tables 5 and 6), the cation distributions are Ti, Mg and Nb at $X1$, the smallest octahedrally coordinated sites, and then this site was filled up by Zr. Due to its relatively long bond distances (2.489 Å) the $X2$ site was occupied by Ca and Na, according to the site-scattering value. The site $X3$ was then filled by the bivalent cations (Fe, Ca and Mn) and the remaining amount of Zr. The $W1$ (O4) and $W2$ (F) sites have been refined as fully occupied by O and F, respectively. The bond-valence sum values confirm these occupancies (Table 7). According to the EPMA, F is slightly in excess in comparison to the ideal value and is assumed to be incorporated at the $W1$ site. The structural formula obtained from the refinement is $^{X4}(Na)_2 {}^{X2}(Ca_{0.85}Na_{0.15})_2 {}^{X3}(Fe_{0.48}Mn_{0.25}Ca_{0.25}Zr_{0.02})_2$ $^{X1}(Ti_{0.85}Zr_{0.07}Nb_{0.04}Mg_{0.04})_2(Si_2O_7)_2(F_{2.16}O_{1.84})$, in good agreement with the empirical chemical formula based on the EPMA data.

Pilanesbergite is isomorphic with the wöhlerite group minerals låvenite ($Na_2Ca_2Mn_2Zr_2(Si_2O_7)_2O_2F_2$), normandite ($Na_2Ca_2Mn_2Ti_2(Si_2O_7)_2O_2F_2$) and madeiraite ($Na_2Ca_2Fe_2Zr_2(Si_2O_7)_2O_2F_2$). The chemical compositions of those mineral species are related through the homovalent chemical substitutions $Mn^{2+} \leftrightarrow Fe^{2+}$ on $X3$ and $Zr^{4+} \leftrightarrow Ti^{4+}$ on $X1$ (Fig. 4 and Table 8). According to the chemical data available in the literature, the solid-solution reactions between the four end-members seem to be complete. It is worth mentioning that the $X3$ site can host a significant amount of Ca^{2+}, in substitution of Mn^{2+} or Fe^{2+}. This is especially the case in the sample of normandite from Mont-Saint-Hilaire, Quebec (Perchiazzi et al., 2000), in madeiraite (Mills et al., 2021) and in pilanesbergite with 0.22, 0.36 and 0.25 ^{X3}Ca pfu, respectively. Consequently, it is likely that a mineral with the hypothetical end-member formula $Na_2Ca_2Ca_2Zr_2(Si_2O_7)_2O_2F_2$ and crystallizing in the låvenite unit-cell setting occurs in nature.

The crystal-chemical features observed for pilanesbergite are in line with those reported for låvenite, normandite and madeiraite. The heterovalent substitution $Ca^{2+} \leftrightarrow Na^+$ occurring on the larger sites is common in those minerals and is usually accompanied by the substitution $Zr^{4+} \leftrightarrow Nb^{5+}$ and $O^{2-} \leftrightarrow F^-$, the latter mechanism being the principal one in the case of pilanesbergite. Finally, the geometry of the octahedral $X1$ site in pilanesbergite is also characterized by five short and one long bonds, as observed in the structure of låvenite, normandite and madeiraite. As mentioned by Perchiazzi et al. (2000), the TiO_6 octahedron tends to show more off-centre displacement (difference between the mean short bond and long bond) than the ZrO_6 octahedron. In pilanesbergite the mean short distance is 1.937 Å and the long distance is 2.319 Å (Table 6), very close to the values reported for normandite from Mont-Saint-Hilaire (1.943 and 2.303 Å), both samples hosting almost the same ^{X1}Ti content. Normandite from Amdrup Fjord, Greenland, has significantly less Ti and more Zr incorporated on its $X1$ site, resulting in a mean short distance of 1.979 Å and a long distance of 2.271 Å. The off-centre displacement is even less in Zr-dominant species such as madeiraite, where the mean

Table 2. Powder X-ray diffraction data for pilanesbergite (d values in Å).

I_{meas}	d_{meas}	d_{calc}	I_{calc}	h k l	I_{meas}	d_{meas}	d_{calc}	I_{calc}	h k l
13	6.684	6.668	9	0 0 1	15	2.324	2.327	3	0 3 2
16	5.496	5.505	2	0 1 1			2.321	4	2 0 −3
13	5.458	5.472	6	1 1 −1	10	2.269	2.264	6	4 2 0
13	5.113	5.110	6	2 0 0	10	2.161	2.167	5	0 1 3
6	4.857	4.878	2	0 2 0	9	2.152	2.154	6	3 3 −2
6	4.518	4.527	< 1	2 1 0	–	–	2.102	1	5 1 −1
–	–	4.402	1	1 2 0	–	–	2.011	1	2 4 1
–	4.346	4.346	< 1	2 1 −1	11	2.006	2.009	6	4 3 0
17	3.928	3.925	11	1 2 −1	12	1.970	1.968	3	0 4 2
–	–	3.554	2	2 0 1			1.963	7	2 3 2
–	–	3.528	3	2 2 0	7	1.947	1.945	4	4 3 −2
16	3.348	3.340	6	2 1 1	–	–	1.917	2	1 5 0
60	**3.219**	3.216	29	3 1 0	6	1.869	1.870	3	1 4 2
–	–	3.130	2	2 1 −2	8	1.863	1.865	3	4 2 −3
12	3.107	3.098	2	1 3 0	14	1.757	1.755	21	2 0 −4
6	2.923	2.923	3	0 3 1			1.752	2	3 3 2
100	**2.851**	2.848	100	1 2 −2	10	1.734	1.735	14	5 3 −2
51	**2.802**	2.793	67	3 2 0			1.732	1	2 4 2
–	–	2.752	7	0 2 2	9	1.732	1.731	2	5 3 0
		2.743	6	2 3 0			1.730	2	1 3 3
27	**2.743**	2.736	8	2 2 −2	**19**	**1.723**	1.721	16	4 4 −2
		2.713	3	1 3 1	–	–	1.693	1	3 5 0
10	2.688	2.682	4	4 0 −1	–	–	1.684	2	1 4 −3
7	2.587	2.589	< 1	4 1 −1	14	1.681	1.681	10	2 4 −3
6	2.472	2.472	10	4 1 0	–	–	1.626	6	0 6 0
		2.439	3	0 4 0	14	1.619	1.615	7	3 1 3
19	**2.423**	2.427	10	4 0 −2	–	–	1.555	3	3 2 3
		2.399	4	2 3 1	–	–	1.549	2	1 1 4
9	2.385	2.385	9	1 3 −2	–	–	1.539	2	6 0 1
9	2.385	2.385	9	1 3 −2	–	–	1.529	8	1 3 −4
18	2.366	2.369	7	3 2 1	10	1.509	1.509	6	6 3 0
–	–	2.352	2	3 3 0					

Calculated intensities were obtained by the VESTA 3 software (Momma and Izumi, 2011), and calculated d values were obtained with the LCLSQ8N software (Burnham, 1991). The six strongest Bragg reflections are in bold.

Table 3. Data collection and structure refinement details for pilanesbergite.

Crystal data	
Temperature (K)	293
Cell setting	Monoclinic
Space group	$P2_1/a$ (No. 14)
a (Å)	10.7811(2)
b (Å)	9.7836(1)
c (Å)	7.0348(1)
β (°)	108.072(2)
V (Å^3)	705.41(2)
Z	2
Calculated density (g cm^{-3})	3.49
Crystal size (mm)	$0.065 \times 0.043 \times 0.025$
Crystal form	Blocky crystal
Crystal colour	Orange

Data collection	
Diffractometer	Rigaku XtaLAB Synergy-S with hybrid photon counting detector (50 kV, 1 mA)
Radiation; λ	MoK_α; 0.71073
Absorption coefficient, μ (mm^{-1})	3.857
$F(000)$	709
θ range (°)	2.88–37.88
Index range	$-18 < h < 18, -16 < k < 16, -11 < l < 12$
No. of measured reflections	34 780
Total reflections (N_{tot})/unique(N_{ref})	3692/3214
Criterion for observed reflections	$I > 3\sigma(I)$

Refinement	
Refinement on	Full-matrix least squares on F^2
R, wR ($I > 3\sigma(I)$)	0.0206, 0.0250
R_2, wR_2 (all reflection)	0.0767, 0.0798
R_{int}	0.04
No. of refinement parameters (N_{par})	139
Weight scheme	$1/(\sigma^2|F| + 0.0036F^2)$
Min./max. residual e density, (e Å^{-3})	$-0.50/0.49$
Goodness of fit (obs/all)	1.04/1.08
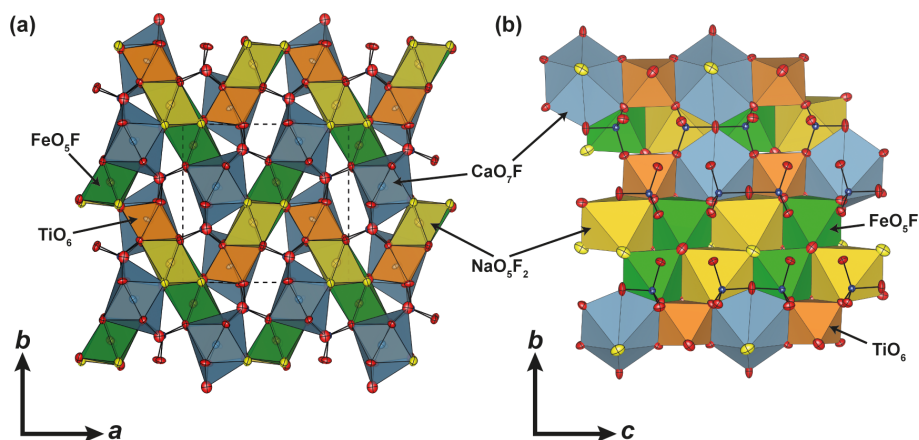
Figure 3. Representation of the crystal structure of pilanesbergite **(a)** across and **(b)** along the c axis. Silicon, oxygen and fluorine atoms are represented by blue, red and yellow spheres, respectively. The dashed lines represent one unit cell, and the displacement ellipsoids represent the 90 % probability level.

short distance is 2.075 Å and a long distance 2.264 Å (Mills et al., 2021).

6.2 Stability and genesis of pilanesbergite: petrological implications

The factors that stabilize agpaitic mineral assemblages have been discussed for more than a century. While elevated peralkalinity is an important driving force, elevated halogen contents are also required to stabilize F-bearing Zr and Ti disilicate minerals and Cl-bearing eudialyte (e.g. Andersen et al., 2010; Marks et al., 2011). The role of water is less clear – agpaitic nepheline syenite magmas are generally not water saturated, but some agpaitic, magmatic mineral assemblages are sensitive to water activity (e.g. Andersen and Sørensen, 2005; Andersen and Friis, 2015). In the green foyaite of the Pilanesberg Complex, Na–Ti–Zr disilicate minerals were in general stabilized relative to titanite and Ti–Zr-bearing aegirine by increasing oxygen fugacity and alkalinity, with progressive crystallization of an agpaitic nepheline syenite magma under relatively dry conditions (Andersen et al., 2018).

The lack of thermodynamic data for pilanesbergite and many of its coexisting mineral species prevents quantitative thermodynamic modelling of its conditions of formation, but the application of chemographic analysis of local low-variance mineral-melt equilibria, which can be visualized in semiquantitative log-activity (or chemical potential) diagrams, may still allow important parameters to be constrained. For a formal development of this method, see Patiño Douce (2011); an introduction to its use in alkaline rocks was given by Andersen et al. (2010).

The observation that the sample carrying pilanesbergite (MEPB62) is heterogeneous with respect to Ti-bearing mineral assemblages (Fig. 2) allows the crystallization history of pilanesbergite to be worked out in some detail and the factors controlling the development to be identified. The mineral associations shown in Fig. 2 correspond to a succession of mineral assemblages involving pilanesbergite, major, Ti-free rock forming minerals that are listed in Tables S1 and S2 in the Supplement, and a silicate liquid.

Phase reactions relating the different mineral assemblages in Table S2 can be modelled in the 10-component system $NaO_{0.5}$-$KO_{0.5}$-CaO-FeO-$FeO_{1.5}$-TiO_2-$AlO_{1.5}$-SiO_2-$HO_{0.5}$-$FO_{-0.5}$. The relative stability relationships can conveniently be illustrated by a grid in $\log a_{Nds} - \log a_{H_2O} - \log f_{O_2}$ space at constant temperature and pressure (Andersen et al., 2018). At constant pressure and temperature, an assemblage of eight phases (five Ti-free and two Ti-bearing minerals plus a silicate liquid) define a divariant assemblage that can be represented by a plane in 3D log activity space, whose orientation is given by the ratios of stoichiometric coefficients of the corresponding phase reaction (Table S3). The resulting diagram (Fig. 5a) is semiquantitative, in the sense that the orientations of divariant planes and univariant lines are

Table 4. Fractional atom coordinates and equivalent isotropic displacement parameters (Å^2) for pilanesbergite.

| Site	x	y	z	U_{eq}
$X1$ (Ti)	0.28191(2)	0.10106(2)	0.02045(3)	0.00650(5)
$X2$ (Ca)	0.30027(3)	0.10756(3)	0.52459(4)	0.00926(7)
$X3$ (Fe)	0.43715(2)	0.36639(2)	0.86007(3)	0.349(4)
$X4$ (Na)	0.42439(5)	0.37788(6)	0.33626(8)	0.0120(1)
Si1	0.62042(3)	0.16487(3)	0.20941(4)	0.00606(8)
Si2	0.62118(3)	0.16640(3)	0.67115(4)	0.00588(8)
O1	0.64295(9)	0.1602(1)	0.4510(1)	0.0147(2)
O2	0.73979(8)	0.26474(8)	0.2018(1)	0.0100(2)
O3	0.74625(8)	0.25631(9)	0.8000(1)	0.0108(2)
O4	0.65304(9)	0.01044(8)	0.1591(1)	0.0110(2)
O5	0.63374(9)	0.00821(9)	0.7418(1)	0.0116(2)
O6	0.47684(8)	0.22080(9)	0.0951(1)	0.0100(2)
O7	0.48380(8)	0.23604(9)	0.6491(1)	0.0111(2)
O8 ($W1$)	0.12611(9)	0.0245(1)	−0.0420(1)	0.0138(2)
F ($W2$)	0.10991(8)	0.00411(8)	0.3988(1)	0.0167(2)
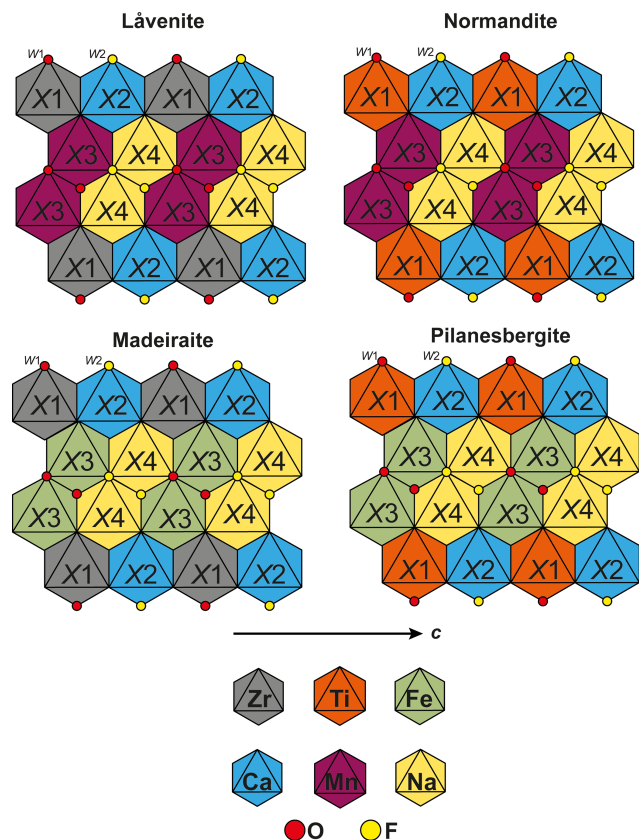
Figure 4. Comparison of the cationic distribution in the so-called octahedral wall occurring in the structure of låvenite, normandite, madeiraite and pilanesbergite.

Table 5. Cation distribution in the crystal structure of pilanesbergite.

Site	RSS (e^-)	Site occupancy	CSS (e^-)	ABL (Å)	CBL (Å)
$^{[6]}X1$	22.62(3)	$Ti_{0.85}Zr_{0.07}Mg_{0.04}Nb_{0.04}$	23.6	2.001	2.019
$^{[8]}X2$	18.70(6)	$Ca_{0.85}Na_{0.15}$	18.7	2.489	2.549
$^{[6]}X3$	23.91(10)	$Fe_{0.48}Ca_{0.25}Mn_{0.25}Zr_{0.02}$	24.5	2.202	2.125
$^{[8]}X4$	11.0	$Na_{1.00}$	11.0	2.562	2.440

RSS: refined site-scattering value normalized to unity; CSS: calculated site scattering value normalized to unity; ABL: average observed bond lengths; CBL: calculated bond lengths. Ideal bond distances are calculated using the ionic radii of Shannon (1976).

Table 6. Selected bond distances and angles for pilanesbergite.

Bond	Distance, Å	Bond	Distance, Å
$X1–O2$	1.979(1)	$X2–O1$	2.683(1)
$X1–O3$	2.032(1)	$X2–O1$	2.786(1)
$X1–O4$	1.956(1)	$X2–O2$	2.495(1)
$X1–O5$	1.955(1)	$X2–O3$	2.563(1)
$X1–O6$	2.319(1)	$X2–O4$	2.417(4)
$X1–O8$	1.765(1)	$X2–O5$	2.476(1)
$\langle X1–O\rangle$	2.001	$X2–O7$	2.278(1)
		$X2–F$	2.212(1)
		$\langle X2–\phi\rangle$	2.489
$X3–O3$	2.306(1)	$X4–O1$	3.007(1)
$X3–O6$	2.123(1)	$X4–O2$	2.374(1)
$X3–O7$	2.132(1)	$X4–O4$	3.007(1)
$X3–O8$	2.212(1)	$X4–O6$	2.481(1)
$X3–O8$	2.245(1)	$X4–O7$	2.511(1)
$X3–F$	2.195(1)	$X4–O8$	2.437(1)
$\langle X3–\phi\rangle$	2.202	$X4–F$	2.232(1)
		$X4–F$	2.358(1)
		$\langle X4–\phi\rangle$	2.562
$Si1–O1$	1.641(1)	$Si2–O1$	1.638(1)
$Si1–O2$	1.630(1)	$Si2–O3$	1.629(1)
$Si1–O4$	1.615(1)	$Si2–O5$	1.618(1)
$Si1–O6$	1.603(1)	$Si2–O7$	1.593(1)
$\langle Si1–O\rangle$	1.622	$\langle Si2–O\rangle$	1.619

$\phi = O^{2-}$ or F^-.

Table 7. Bond valences (valence units) for pilanesbergite.

	$X1$	$X2$	$X3$	$X4$	Si1	Si2	$\sum$
O1		0.14 0.10		0.03	0.95	0.96	2.19
O2	0.65	0.22		0.21	0.99		2.08
O3	0.57	0.19	0.26			0.99	2.00
O4	0.70	0.28		0.04	1.02		2.04
O5	0.70	0.24				1.02	1.95
O6	0.26		0.43	0.16	1.05		1.91
O7		0.40	0.42	0.15		1.08	2.05
O8 ($W1$)	1.17		0.34 0.31	0.18			1.99
F1 ($W2$)		0.35	0.27	0.22 0.16			1.00
$\sum$	4.04	1.91	2.03	1.15	4.02	4.05	
VS	3.96	1.85	2.04	1.00	4.00	4.00	

Bond-valence parameters are recalculated according to the site occupancies (see Table 6), and taken from Brown and Altermatt (1985) for the all the cations apart Si, for which the parameters from Gagné and Hawthorne (2015) have been used. VS: expected valence calculated from the empirical formula.

fixed, whereas sizes of volumes and the absolute position of volumes, lines and planes in log activity space are unconstrained. The relative positions of planes, lines and volumes are constrained by petrographic observation and in obedience to Schreinemaker's rules (e.g. Zen, 1966). Titanium enrichment in aegirine can best be represented by the $NaFe^{2+}_{0.5}Ti_{0.5}Si_2O_6$ component (*TiAeg* in Table S1). Reactions involving this component are not formally divariant, and the corresponding planes may be translated parallel to the $\log a_{Nds}$ axis of the diagram, depending on Ti content in aegirine. Beyond this, the geometry of the diagram is unaffected.

The stability of pilanesbergite must be evaluated relative to mineral assemblages with aenigmatite, titanite and Ti-enriched aegirine. Lorenzenite formed as a late mineral in the sample that cannot be directly related to pilanesbergite and the other Ti minerals. A water-undersaturated silicate liquid and the minerals nepheline, albite, potassium feldspar, aegirine and arfvedsonite are present in all assemblages with titanite, aenigmatite, pilanesbergite and Ti-enriched aegirine (Table S2). End-member mineral compositions have been used in the model calculations, except for arfvedsonite, where the observed, potassic composition has been used (Table S1). Divariant reactions have been balanced and plane orientations determined using a matrix inversion routine implemented in Microsoft Excel 2016/VBA, and geometric constructions in isometric 3D space were done in Autocad 2023.

The stability grid in log activity space. The 3D stability grid for the Ti-bearing minerals (Fig. 5a) is dominated by

Table 8. Comparison of pilanesbergite with closely related minerals.

	Pilanesbergite	Låvenite	Normandite*	Madeiraite
Formula	$Na_2Ca_2Fe_2Ti_2$ $(Si_2O_7)_2O_2F_2$	$Na_2Ca_2Mn_2Zr_2$ $(Si_2O_7)_2O_2F_2$	$Na_2Ca_2Mn_2Ti_2$ $(Si_2O_7)_2O_2F_2$	$Na_2Ca_2Fe_2Zr_2$ $(Si_2O_7)_2O_2F_2$
Unit-cell parameters				
a (Å)	10.7811(1)	10.8475(6)	10.798(1)	10.880(1)
b	9.7836(1)	9.9364(6)	9.835(1)	10.0442(7)
c	7.0348(1)	7.1788(4)	7.090(2)	7.2250(7)
β (°)	108.072(2)	108.392(4)	108.08(3)	108.78(1)
V (Å^3)	705.41(2)	731.17(7)	715.77(3)	747.54(7)
Optical properties				
Biaxial	(+)	(−)	(−)	(−)
α	1.743(3)	1.670	1.743(2)	1.690(5)
β	1.768(3)	1.690	1.785(2)	1.707(5)
γ	1.795(5)	1.720	1.810(5)	1.720(5)
$2V$ (°)	88	40–70	72–84	83
Cation distribution				
$X1$	$Ti_{0.85}Zr_{0.07}Mg_{0.04}Nb_{0.04}$	$Zr_{0.74}Nb_{0.19}Ti_{0.07}$	$Ti_{0.88}Nb_{0.12}$	$Zr_{0.80}Ti_{0.12}Nb_{0.08}$
$X2$	$Ca_{0.85}Na_{0.15}$	$Ca_{0.58}Na_{0.42}$	$Ca_{0.72}Na_{0.28}$	$Ca_{0.55}Na_{0.45}$
$X3$	$Fe_{0.48}Ca_{0.25}Mn_{0.25}Zr_{0.02}$	$Mn_{0.67}Ti_{0.16}Fe_{0.14}$ $Ca_{0.02}Mg_{0.01}$	$Mn_{0.78}Ca_{0.22}$	$Fe_{0.43}Ca_{0.36}Ti_{0.12}$ $Mn_{0.05}Mg_{0.02}Y_{0.02}$
$X4$	$Na_{01.00}$	$Na_{1.00}$	$Na_{1.00}$	$Na_{0.80}Ca_{0.20}$
References	This proposal	Biagioni et al. (2012) Perchiazzi et al. (2000)	Chao and Gault (1997)	Mills et al. (2021)

* The crystal-chemical data are reported for normandite from the type locality, Mont-Saint-Hilaire, Canada.
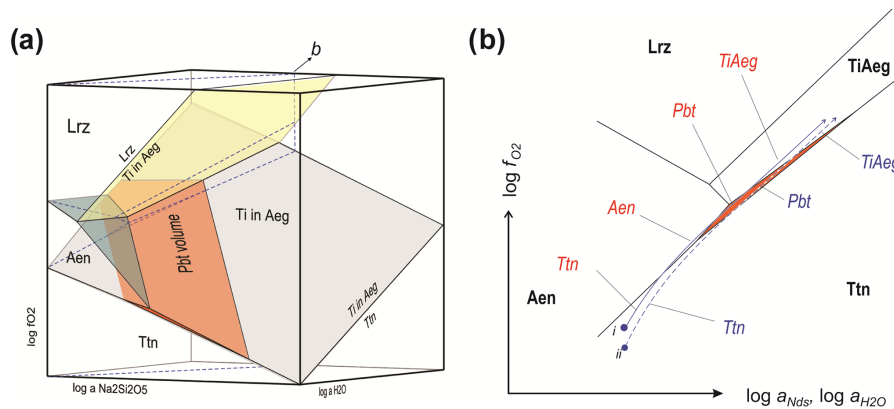
Figure 5. (a) Petrogenetic grid in 3D $\log a_{Nds} - \log a_{H_2O} - \log f_{O_2}$ space for pilanesbergite and other Ti-bearing minerals in sample MEPB62. Albite, K-feldspar, nepheline, aegirine and potassic arfvedsonite are additional phases present in all assemblages illustrated. Mineral compositions are given in Table S1, the full assemblages in Table S2 and the reactions defining divariant planes in Table S3. Dashed blue lines mark the intersection with a plane that corresponds to evolution of an agpaitic magma at a moderate increase in a_{Nds}. **(b)** Detail showing the intersection of the plane marked "b" in **(a)** with the stability volumes of Ti-bearing minerals in sample MEPB62. The scale is exaggerated in the vertical direction for clarity. The intersection with the stability volume of pilanesbergite is shown with orange shading, the others with phase indicators.
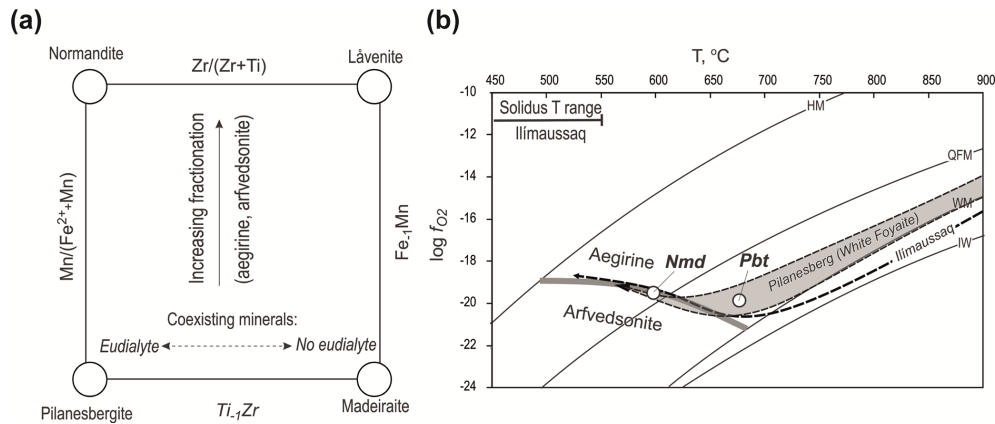
Figure 6. (a) Relationships of pilanesbergite with the other låvenite-related minerals in the wöhlerite group and the two independent substitutions mechanisms involving Mn^{2+} and Fe^{2+} on $X3$ and Ti^{4+} and Zr^{4+} on $X1$. **(b)** $T-f_{O_2}$ evolution trend for nepheline syenite in the Pilanesberg Complex (Andersen et al., 2017), with stability fields of aegirine and arfvedsonite and with the crystallization conditions of pilanesbergite and normandite indicated. See further explanation in the text.

large stability volumes of titanite at low f_{O_2} and titanium-enriched aegirine at elevated f_{O_2} and a_{Nds}. Aenigmatite is stable at intermediate f_{O_2} levels at low a_{Nds}, and a lorenzenite volume is situated at low a_{Nds} and elevated a_{H_2O} and f_{O_2}. This lorenzenite volume does not, however, represent conditions of crystallization of late lorenzenite with natrolite in the sample. The stability field of pilanesbergite forms an inclined wedge that is narrow in log f_{O_2} direction, separating the volumes of titanite and Ti-enriched aegirine and moderate to high a_{Nds}. Towards low a_{Nds} it is truncated by the aenigmatite and lorenzenite volumes. The inclination of the volume is such that pilanesbergite will be stable at very high a_{Nds} only at low f_{O_2} and a_{H_2O}.

The succession of Ti-bearing mineral assemblages seen in the sample (Fig. 2 and Table S2) can be accounted for by a moderate increase in a_{Nds} coupled with increasing a_{H_2O} and f_{O_2}. Figure 5b shows two trends of evolution for systems starting crystallizing titanite and ending with Ti hosted by aegirine in the plane marked "b" in Fig. 5a. Depending on locally controlled oxygen fugacity by co-crystallizing minerals, parts of the system can evolve along slightly different paths in the plane, sufficiently different to cause distinct successions of stable mineral assemblages. At increasing f_{O_2} and a_{H_2O}, the path of evolution of system starting at point (i) in the diagram may crystallize titanite, followed by aenigmatite, pilanesbergite and Ti-rich aegirine, i.e. the full sequence of assemblages in Table S2. In Fig. 2, this corresponds to a trend from assemblages seen in panel (e) through (a), (b) and finally (f). For a domain with slightly lower initial oxygen fugacity (point ii in Fig. 5), the trend will not intersect the aenigmatite field, and the succession will be titanite followed by pilanesbergite and finally Ti-enriched aegirine (assemblages 1–3–4–5), as seen in Fig. 2c, followed by Fig. 2d and f.

Pilanesbergite and related Fe–Mn–Ti–Zr silicate mineral. The four minerals *pilanesbergite, normandite, madeiraite and låvenite* are structurally and chemically related (Dal Bo et al., 2022). They have extensive mutual solubility, controlled by the two simple substitution mechanisms $Fe^{2+}_{-1}Mn$ in the $X3$ site and $Ti_{-1}Zr$ in $X1$ (Fig. 6a). Since both of these substitutions are charge-balanced, no coupling between them is required. The composition of the mineral will be influenced by factors such as melt composition and the physical conditions of crystallization. The $Mn/(Fe^{2+} + Mn)$ ratio of the mineral will reflect the differentiation status of the magma: fractionation of aegirine and/or arfvedsonite will remove iron and thereby increase the $Mn/(Fe^{2+} + Mn)$ of the residual liquid. Furthermore, the $Mn/(Fe^{2+} + Mn)$ ratio will respond to changes in oxygen fugacity due to fractionation in a closed system. The $T-f_{O_2}$ path of evolution for nepheline syenite in the Pilanesberg Complex (Fig. 6b) has an early stage at low oxygen fugacity, followed by an increase in f_{O_2} relative to buffer curves during late magmatic crystallization (Andersen et al., 2017). This crystallization trend mimics that described from the Ilímaussaq Complex, South Greenland (Markl et al., 2001), and represents the response of oxygen fugacity to changes in Fe^{3+}/Fe^{2+} due to fractionation in a closed, internally oxygen-buffered agpaitic nepheline syenite magma crystallizing aegirine, followed by aegirine plus arfvedsonite. The early, aegirine-dominated part of the trend has a low oxygen fugacity level because the Fe^{3+}/Fe^{2+} ratio is kept low by removal of aegirine. Subsequent co-crystallization of arfvedsonite ($Fe^{2+}/Fe^{3+} = 1/4$) causes an increase in Fe^{3+}/Fe^{2+} in the residual liquid and an increase in oxygen fugacity relative to buffer curves. This further reduces the amount of Fe^{2+} available, enhancing the trend towards manganese-rich mineral compositions, i.e. from *Pbt* to *Nmd* (Fig. 6b). The $Ti_{-1}Zr$ substitution is independent of oxygen fugacity, but it will respond to fractionation of the

Ti/Zr ratio of the residual melt. Ti is commonly a minor element (> 1 wt % TiO_2) and Zr an abundant trace element (> 1000 ppm). However, the controlling factor is more likely to be coexisting mineral assemblage rather than bulk composition. Zirconium-rich eudialyte-group minerals (EGMs) are characteristic, rock-forming minerals in agpaitic nepheline syenite that commonly exclude Ti. A disilicate mineral coexisting with a Zr-rich EGM is therefore likely to acquire a high Ti/(Ti + Zr) ratio, as is seen in MEPB62. However, crystallization of eudialyte requires a higher degree of peralkalinity than disilicate minerals and also elevated chlorine activity (Andersen et al., 2010). If either of these factors is insufficient to stabilize EGMs, Zr will not be removed from the residual liquid, and disilicate minerals will be Zr-enriched, i.e. låvenite and madeiraite rather than pilanesbergite and normandite.

Andersen et al. (2018) reported normandite with Mn/(Mn + Fe) > 1 as part of an *Aeg + Arf* assemblage in green foyaite from the Pilanesberg Complex. This mineral assemblage is characteristic of a relatively advanced stage of evolution, following early stages of crystallization with *Aen–Eud–Aeg* assemblages without *Arf* or *Nmd*. Normandite crystallization in Pilanesberg can thus be assigned to the late, increasing the f_{O_2} part of the crystallization trend shown in Fig. 6b, whereas pilanesbergite in the MEPB62 sample formed at an earlier stage, prior to significant fractionation of arfvedsonite.

References

Andersen, T. and Friis, H.: The Transition from Agpaitic to Hyperagpaitic Magmatic Crystallization in the Ilímaussaq Alkaline Complex, South Greenland, J. Petrol., 56, 1343–1364, https://doi.org/10.1093/petrology/egv039, 2015.

Andersen, T. and Sørensen, H.: Stability of naujakasite in hyperagpaitic melts, and the petrology of naujakasite lujavrite in the Ilímaussaq alkaline complex, South Greenland, Mineral. Mag., 69, 125–136, https://doi.org/10.1180/0026461056920240, 2005.

Andersen, T., Erambert, M., Larsen, A. O., and Selbekk, R. S.: Petrology of nepheline syenite pegmatites in the Oslo Rift, Norway: Zirconium silicate mineral assemblages as indicators of alkalinity and volatile fugacity in mildly agpaitic magma, J. Petrol., 51, 2303–2325, https://doi.org/10.1093/petrology/egq058, 2010.

Andersen, T., Elburg, M. A., and Erambert, M.: The miaskitic-to-agpaitic transition in peralkaline nepheline syenite (white foyaite) from the Pilanesberg Complex, South Africa, Chem. Geol., 455, 166–181, https://doi.org/10.1016/j.chemgeo.2016.08.020, 2017.

Andersen, T., Elburg, M. A., and Erambert, M.: Contrasting trends of agpaitic crystallization in nepheline syenite in the Pilanesberg Complex, South Africa, Lithos, 312–313, 375–388, https://doi.org/10.1016/j.lithos.2018.05.015, 2018.

Biagioni, C., Merlino, S., Parodi, G. C., and Perchiazzi, N.: Crystal chemistry of minerals of the wöhlerite group from the Los Archipelagos, Guinea, Can. Mineral., 50, 593–609, https://doi.org/10.3749/canmin.50.3.593, 2012.

Brown, I. D. and Altermatt, D.: Bond-valence parameters obtained from a systematic analysis of the Inorganic Crystal Structure Database, Acta Crystallogr. B, 41, 244–247, 1985 (with updated parameters from http://www.ccp14.ac.uk/ccp/web-mirrors/i_d_brown/, last access: 21 September 2023).

Burnham, C. W.: LCLSQ: Lattice parameter refinement using correction terms for systematic errors, Am. Mineral., 76, 663–664, 1991.

Cawthorn, R. G.: The geometry and emplacement of the Pilanesberg Complex, South Africa, Geol. Mag., 152, 802–812, https://doi.org/10.1017/S0016756814000764, 2015.

Chao, G. Y. and Gault, R. A.: Normandite, the Ti-analogue of låvenite from Mont Saint-Hilaire, Quebec, Can. Mineral., 35, 1035–1039, 1997.

Dal Bo, F., Friis, H., and Mills, S. J.: Nomenclature of wöhlerite-group minerals, Mineral. Mag., 86, 661–676, https://doi.org/10.1180/mgm.2022.10, 2022.

Elburg, M. and Cawthorn, R. G.: Source and evolution of the alkaline Pilanesberg Complex, Chem. Geol., 455, 148–165, https://doi.org/10.1016/j.chemgeo.2016.10.007, 2017.

Gagné, O. C. and Hawthorne, F. C.: Comprehensive derivation of bond-valence parameters for ion pairs involving oxygen, Acta Crystallogr. B, 71, 562–578, https://doi.org/10.1107/S2052520615016297, 2015.

Mandarino, J. A.: The Gladstone-Dale relationship: part IV. The compatibility concept and its application, Can. Mineral., 19, 441–450, 1981.

Markl, G., Marks, M., Schwinn, G., and Sommer, H.: Phase equilibrium constraints on intensive crystallization parameters of the Ilímaussaq Complex, South Greenland, J. Petrol., 42, 2231–2258, https://doi.org/10.1093/petrology/42.12.2231, 2001.

Marks, M. A. W., Hettmann, K., Schilling, J., Frost, B. R., and Markl, G.: The Mineralogical Diversity of Alkaline Igneous Rocks: Critical Factors for the Transition from Miaskitic to Agpaitic Phase Assemblages, J. Petrol., 52, 439–455, https://doi.org/10.1093/petrology/egq086, 2011.

Mellini, M.: Refinement of the crystal structure of låvenite, Tscher. Miner. Petrog., 28, 99–112, 1981.

Mills, S. J., Dal Bo, F., Alves, P., Friis, H., and Missen, O. P.: Madeiraite, IMA 2021-077, in: CNMNC Newsletter 64; Mineral. Mag., 85, 178–182, https://doi.org/10.1180/mgm.2021.93, 2021.

Momma, K. and Izumi, F.: VESTA 3 for three-dimensional visualization of crystal, volumetric and morphology data, J. Appl. Crystallogr., 44, 1272–1276, https://doi.org/10.1107/S0021889811038970, 2011.

Oxford diffraction: Crys Alis PRO. Oxford Diffraction Ltd, Abingdon, Oxfordshire, England, 2006.

Palatinus, L. and Chapuis, G.: Superflip – a computer program for the solution of crystal structures by charge flipping in arbitrary dimensions, J. Appl. Crystallogr., 40, 451–456, https://doi.org/10.1107/S0021889807029238, 2007.

Patiño Douce, A.: Thermodynamics of the Earth and planets, Cambridge University Press, Cambridge, https://doi.org/10.1017/CBO9780511974854, 2011.

Perchiazzi, N., McDonald, A. M., Gault, R. A., Johnsen, O., and Merlino, S.: The crystal structure of normandite and its crystal-chemical relationships with låvenite, Can. Mineral., 38, 641–648, https://doi.org/10.2113/gscanmin.38.3.641, 2000.

Petříček, V., Dušek, M., and Palatinus, L.: Crystallographic Computing System Jana 2006: general features, Z. Kristallogr., 229, 345–352, https://doi.org/10.1515/zkri-2014-1737, 2014.

Pouchou, J.-L. and Pichoir, F.: Quantitative analysis of homogeneous or stratified microvolumes applying the model "PAP", in: Electron Probe Quantitation, edited by: Heinrich, K. F. J. and Newbury, D. E., Plenum Press, New York, 31–75, https://doi.org/10.1007/978-1-4899-2617-3_4, 1991.

Shannon, R. D.: Revised effective ionic radii and systematic studies of interatomic distances in halides and chalcogenides, Acta Crystallogr. A, 32, 751–767, 1976.

Solem, M. F.: Controls on the REE patterns in sodic pyroxenes in the Green Foyaite from the Pilanesberg Complex, South Africa, MSc thesis, Department of Geosciences, University of Oslo, 162 pp., https://www.duo.uio.no/handle/10852/70412 (last access: 21 September 2023), 2019.

Zen, E.-A.: Construction of pressure temperature diagrams for multicomponent systems after the method of Schreinemakers – A geometric approach, United States Geological Survey Bulletin 1225, 56 pp., 1966.